ACS APPLIED NANO MATERIALS

www.acsanm.org Article

One-Step Hydrothermal Synthesis of Phase-Engineered MoS_2/MoO_3 Electrocatalysts for Hydrogen Evolution Reaction

Shanmughasundaram Duraisamy,[§] Abhijit Ganguly,[§] Preetam Kumar Sharma, John Benson, James Davis, and Pagona Papakonstantinou*

Cite This: https://dx.doi.org/10.1021/acsanm.0c03274 Read Online

ACCESS | Metrics & More | Article Recommendations | Supporting Information

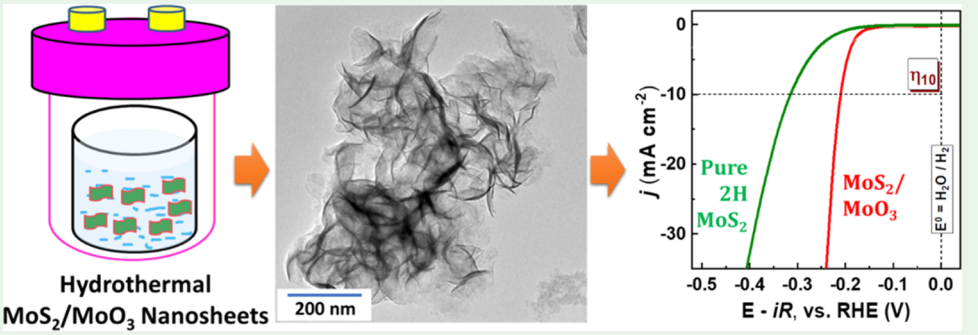

ABSTRACT: The development of suitable approaches for the synthesis of ultrathin transition-metal dichalcogenide (TMD) catalysts is required to engineer phases, intercoupling between different phases, in-plane defects, and edges and hence maximize their catalytic performance for hydrogen production. In this work, we report a simple one-step hydrothermal approach for the synthesis of a three-dimensional (3D) network of self-assembled metallic MoS_2/MoO_3 nanosheets, using α-MoO_3 and thiourea (TU) as the Mo and S precursors, respectively. A systematic structural/property relationship study, while varying the precursors' molar concentration ratios (TU/MoO_3) and reaction temperatures (T_R), revealed a kinetically controlled regime, in hydrothermal synthesis, that enabled the formation of ultrathin branched MoS_2/MoO_3 nanosheets with the highest metallic content of ~47 % in a reproducible manner. Importantly, the work established that in addition to the rich metallic MoS_2 phase (1T), the electronically coupled interfaces between MoO_3 and MoS_2 nanodomains, profusion of active sites, and tuned electrical conductivity significantly contributed to hydrogen evolution reaction (HER)-catalytic activity, affording a low overpotential of 210 mV (with respect to the reversible hydrogen electrode) at a current density of 10 mA/cm^2, a small Tafel slope of ~50 mV/dec, and high stability. Overall, this work demonstrated a controllable one-step hydrothermal method for the rational design and synthesis of a 3D network of MoS_2/MoO_3 nanosheets with high 1T-MoS_2 metallic yield, simultaneous incorporation of MoO_3/MoS_2 heterointerfaces, sulfur vacancies, and tuned electrical conductivity, which are highly beneficial for clean energy conversion applications that can potentially be expanded to other two-dimensional TMD materials.

KEYWORDS: *transition-metal dichalcogenides, molybdenum disulfide-layered materials, metallic phase, hydrothermal synthesis, hydrogen evolution reaction, MoS_2/MoO_3 heterojunction, sulfur vacancies, MoO_{3-x}*

1. INTRODUCTION

Electrochemical generation of hydrogen (H_2) is considered as a green and sustainable way for producing clean alternatives for fossil fuels. Large-scale industrial application of water dissociation is highly dependent on the development of robust electrodes, loaded with active catalysts, that can provide large current densities at low potentials.[1] Pt-based catalysts are undoubtedly the most active for hydrogen evolution reaction (HER) and thus used as a benchmark; however, the high cost and scarcity of Pt have greatly impeded their widespread applications. To this end, many efforts have been devoted to creating cheaper and earth-abundant alternatives.

Recent innovations have demonstrated that the HER activity of two-dimensional (2D)-layered transition-metal dichalcogenides (2D-TMDs) can be considerably improved through transformation of the semiconducting phase to metallic phase.[2−8] A typical representative of 2D-TMDs, MoS_2 possesses different phases, originating from the different

Received: December 7, 2020
Accepted: February 26, 2021

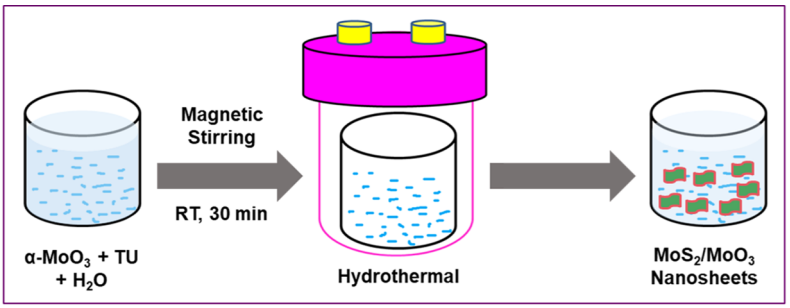

TU/MoO_3 (or S/Mo) Molar Ratio

Sample ID	Thiourea TU (mM)	α-MoO_3 (mM)	T_R (°C)
M1.5	10	15	200
M2.5	10	25	200
M3.5	10	35	200
M4.5	10	45	200
M7.0	10	70	200

Hydrothermal Reaction Temp. T_R

Sample ID	Thiourea, TU (mM)	α-MoO_3 (mM)	T_R (°C)
M160	10	25	160
M180	10	25	180
M200	10	25	200
M220	10	25	220
M240	10	25	240

Figure 1. (Top) Schematic diagram of the proposed hydrothermal synthesis of MoS_2/MoO_3 nanosheets. (Bottom left) List of the samples synthesized with different TU/MoO_3 (or S/Mo) molar concentration ratios (M1.5−M7.0). (Bottom right) List of samples synthesized at different hydrothermal reaction temperatures T_R (M160−M240). The T_R-dependent study was conducted at the optimum precursors' concentration ratio of 2.5 established from the TU/MoO_3 ratio-dependent study.

coordination of Mo and S atoms, including the thermodynamically stable trigonal prismatic 2H phase and the thermally metastable octahedral coordinated 1T phase. The 2H-MoS_2 is the most stable but owing to limited unsaturated S active sites[9] located at its edges and inherently low electrical conductivity of the inactive semiconducting basal plane (S sites in the basal plane are inert), it provides a modest activity for electrochemically catalyzing the hydrogen production. To this end, various efforts[6,10−13] have focused on creating catalytically active sites on the basal plane by introducing sulfur vacancies/defects. Such an approach creates gap states close to the Fermi level and allows hydrogen to bind to the exposed molybdenum atoms directly.

In contrast to the semiconducting 2H phase, 1T-MoS_2 shows metallic characteristics, facilitating fast electron/charge transfer, leading to significantly boosted HER activity. However, to date, it is highly challenging to directly synthesize MoS_2 with the pure 1T phase due to the high formation energies involved. Moreover, the 1T phase is metastable and easily converts into the stable 2H phase at low temperatures. So far, various strategies[2−6,14] have resulted in a limited portion of the 1T phase, mainly relying on phase transformation of 2H to 1T,[2−5] and these include electron beam scanning,[3] ion intercalation (such as Li^+, *tert*-butyllithium,[2,15−20] or NH_4^+),[8,21,22] mechanical strain,[4] and element doping[14,23] of 2H-MoS_2. However, these tactics relying on phase transformation of the already formed 2H-MoS_2 ultimately relate to complex multistep processes of controlling the doping species and defect concentration and, in many cases, require expensive instrumentation or highly toxic reaction sources. Bottom-up approaches, where 1T-MoS_2 in the form of nanopetals is directly formed from Mo and S molecular precursors via low-temperature hydrothermal/solvothermal methods[24,25] in water/ethanol/*N*,*N*-dimethylformamide (DMF), have shown promise; however, their detailed synthesis process has rarely been investigated with a view of understanding their formation mechanism.[26]

From the above discussion, it is implied that both phase and defect engineering of MoS_2 are advantageous for enhancing the electrocatalytic activity.[2,4,6,10−12] Consequently, the synchronized adjustment of the various aspects that control the catalytic activity could lead to the improved design and performance of earth-abundant 2D-TMDs. In this regard, it is highly timely to explore the controlled synthesis of MoS_2 to achieve a large proportion of 1T-MoS_2, coupled with the appropriate defect engineering for boosting HER activity.

In this work, we developed a novel hydrothermal method for the synthesis of MoS_2/MoO_3 nanosheets (NSs) from MoO_3 and thiourea (TU) precursors. Systematic variation of the precursors' molar concentration ratios (TU/MoO_3) and reaction temperature (T_R) allowed control over the crystal phase, enabling the formation of metallic-rich MoS_2-branched few-layered nanosheets incorporating MoS_2/MoO_3 heterostructures in a consistent manner. We report a comprehensive study on the atomic structure (utilizing high-resolution transmission electron microscopy, HRTEM), surface morphology (utilizing field emission scanning electron microscopy, FE-SEM), chemical bonding (utilizing X-ray photoelectron spectroscopy, XPS), crystalline structure (utilizing X-ray diffraction, XRD), and electrocatalytic performance of MoS_2. This is the first time, to the best of our knowledge, that a synthesis/structure/catalytic function triangle relationship of three-dimensional (3D) self-assembled MoS_2/MoO_3 nanosheets is reported, unraveling the evolution of 1T/2H-MoS_2 and Mo oxide phases and their synergetic influence on the electrocatalytic performance. We found that a TU/MoO_3 ratio of 2.5 and a T_R of 200 °C led to the synthesis of MoS_2 nanosheets with the highest metallic content of ∼47 %. This high metallic content together with the synergetic effect of MoS_2/MoO_3 heterojunctions, which afforded high electron transfer as well as the presence of numerous defects such as

https://dx.doi.org/10.1021/acsanm.0c03274
ACS Appl. Nano Mater. XXXX, XXX, XXX−XXX

sulfur vacancies, defects created at the boundary between 1T and 2H nanoscale domains on the basal plane, and oxygen vacancies in MoO_3, contributed positively toward enhanced HER electrocatalytic performance. This study provides new insights into rationally designing efficient electrocatalysts via appropriate modulation of phases and crystalline structures and integrating different functional active sites into material systems.

2. RESULTS AND DISCUSSION

3D self-assembled MoS_2/MoO_3 nanosheets (NSs) with mixed metallic/semiconducting MoS_2 (hereafter called 1T/2H-MoS_2) phases as well as MoO_3 phases were obtained via a simple one-step hydrothermal approach, as depicted in Figure 1 (top panel). A detailed study has been carried out to explore the role of sulfur-to-molybdenum (S/Mo) molar ratio and reaction temperature (T_R) (listed at the bottom panel of Figure 1; more details are provided in Table S1, Supporting Information) on the formation of different phases (1T-MoS_2, 2H-MoS_2, and molybdenum oxide phases, denoted hereafter as MoO_x) and resultant HER electrocatalytic activity in an aqueous acidic medium (0.5 M H_2SO_4).

The S/Mo molar ratio was adjusted by varying the precursors' molar concentration ratios (TU/MoO_3) to 1.5, 2.5, 3.5, 4.5, and 7.0 values. The reaction was carried out at 200 °C for 24 h, and the synthesized samples were labeled as M1.5, M2.5, M3.5, M4.5, and M7.0, respectively. Since the sample M2.5 demonstrated the best HER activity, the 2.5 ratio was chosen for the subsequent T_R-dependent study at temperatures of 160, 180, 200, 220, and 240 °C. The reaction time was kept at 18 hours, and the samples were labeled as M160, M180, M200, M220, and M240, respectively.

2.1. Synthesis of MoS_2: Reaction between MoO_3 and Thiourea (TU). The mechanism underlying the formation of MoS_2 is associated with the anion-exchange and reduction reactions described by the following eqs 1−3[27]

$$NH_2CSNH_2 + 2H_2O \rightarrow H_2S + 2NH_3 + CO_2 \quad (1)$$

$$H_2S + 2OH^- \rightarrow S^{2-} \quad (2)$$

$$MoO_3 + S^{2-} \rightarrow MoS_3\ (\text{intermediate}) \rightarrow MoS_2\ (1T/2H)\ MoS_2 \quad (3)$$

At first, TU (NH_2CSNH_2) undergoes decomposition to produce S^{2-} anions via the hydrolyzation steps, at elevated temperatures, described by eqs 1 and 2. Subsequently, MoS_3 (intermediate byproduct) is formed by a direct anion-exchange reaction between the O^{2-} anion of α-MoO_3 and S^{2-} anions of sulfur.[28] Finally, MoS_3 is immediately reduced to 1T and 2H phases of MoS_2 as the final product (eq 3).

A number of interesting phenomena were observed during the synthesis process. Notably, whereas the initial pH of the solution was found to be within 3.4−3.5 acidic range, the pH became slightly basic (pH: 7−8) after the hydrothermal reaction (Figure S1). In particular, the solution pH after the reaction was found to be sensitive to the precursors' molar concentration ratio (TU/MoO_3), gradually increasing from 7.2 to 8.3 for M1.5−M7.0 (Figure S1a). Overall, the increase in pH is most probably associated with the formation of increased ammonia levels (which is a byproduct of the reaction system, as described by eq 1) being more pronounced at high TU/MoO_3 ratios. We should note that in our study, the observed pH changes were exclusively related to the increase in the thiourea content, which served both as a S source and as a reducing agent. No additional reducing or oxidation agents were employed in this work to adjust the pH of the solution before the reaction. An increase in reaction temperature (T_R) also led to an increment in solution pH, however less pronounced (from 7.5 at 160 °C to 7.8 at 240 °C; Figure S1b), and was associated with a more efficient dissociation of TU and production of ammonia levels at increased temperatures.

Apparent observations were also noted with respect to the dispersion of the reaction products. Samples synthesized at high TU/MoO_3 ratios (M4.5 and M7.0) or those synthesized at high T_R (M220 and M240) exhibited poor dispersion in water, which is an indication of the formation of predominant 2H-MoS_2 phase.[29] Black-colored products were found to settle at the bottom of the hydrothermal reaction vessel for samples M4.5, M7.0, M220, and M240. In contrast, for samples synthesized with low TU/MoO_3 ratios (M1.5, M2.5) or low T_R (M160, M180, M200), black-colored particles were found to be well dispersed in a turbid liquid, indicating hydrophilic nature, most probably due to the presence of the metallic phase in the synthesized MoS_2 products.[30] For visualization purposes, a comparison of optical photos of M200 and M240 products, which were dispersed in water and left to settle for 1 h, is presented in Figure S2a,b. M240 gives a sediment, whereas M200 remains well dispersed indicative of their hydrophobic and hydrophilic nature, respectively.

Hydrothermal synthesis of MoS_2 depends on the solubility of selected precursors at relatively elevated temperature and high pressure in an aqueous solution, allowing controlled nucleation and growth of the molybdenum disulfide phases. The orthorhombic α-MoO_3 has a layered structure, which is formed by stacking bilayer sheets of MoO_6 octahedra with van der Waals forces. Orthorhombic α-MoO_3 was chosen as the Mo source due to the fact that MoO_3 and 1T-MoS_2 share a similar octahedral crystal structure[22,31,32] and has demonstrated potential for increased MoS_2 metallic phase. Prior to hydrothermal reaction, the starting MoO_3 platelets in water formed a white-colored solution indicating the formation of molybdic acid. Under the hydrothermal conditions of high temperature and pressure used in this work, the MoO_3 was completely dissolved. Further confirmation is provided from previous experimental studies,[33,34] which have shown that the solubility of MoO_3 increases with increasing temperature, creating $HMoO_4^-$ species ($MoO_3 + H_2O \leftrightarrow HMoO_4^- + H^+$). It is worth noting that in an experiment, where we stopped the reaction after 1 h, it resulted in a transparent solution, suggesting the complete dissolution of MoO_3 bulk rodlike crystals. SEM images presented later (Figures 2 and S3a) show that the synthesized products do not inherit the rodlike morphology of the original MoO_3 powder. To further confirm the complete dissolution of MoO_3 crystals, we also used exfoliated MoO_3 nanosheets as a precursor. No change in the morphology and electrocatalytic performance was observed between the two Mo precursors, which is another proof that the MoO_3 crystals, either in bulk or in nanosheet form, are dissolved under the high temperature and pressure of the hydrothermal process.

2.2. Morphology, Chemical Composition, and Phase Quantification. *2.2.1. Morphological Study: SEM.* Field emission scanning electron microscopy (FE-SEM) provided evidence of self-assembled 3D networks of nanosheets for the

https://dx.doi.org/10.1021/acsanm.0c03274
ACS Appl. Nano Mater. XXXX, XXX, XXX−XXX

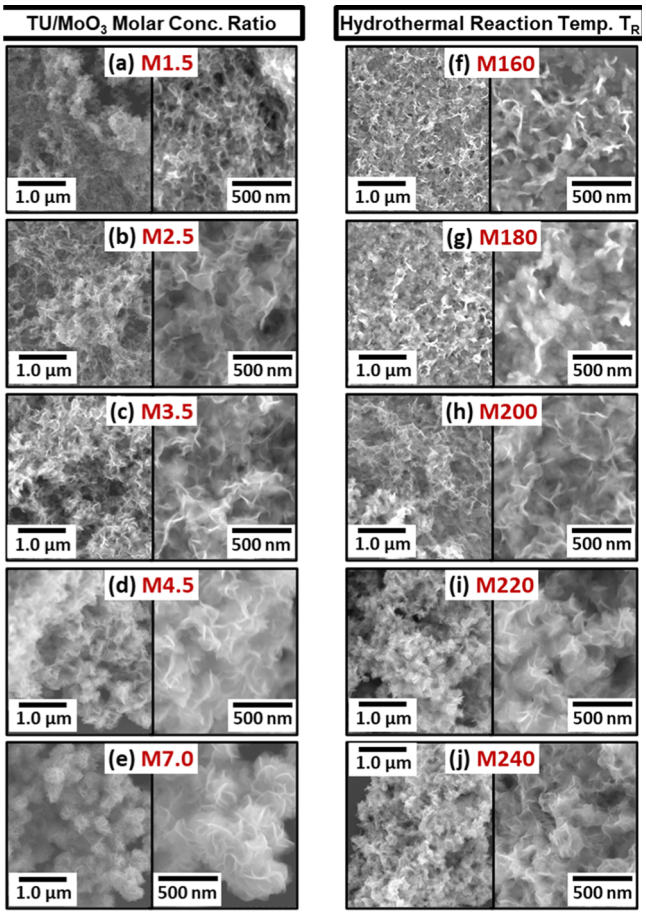

Figure 2. Field emission SEM images of hydrothermally synthesized MoS_2/MoO_3 nanostructured products (a–e) produced with different TU/MoO_3 molar concentration ratios (samples M1.5–M7.0) and (f–j) produced at different hydrothermal reaction temperatures T_R (samples M160–M240).

hydrothermally synthesized products, as illustrated in Figure 2. All synthesized products showed similar morphology of interconnected nanosheets, irrespective of the TU/MoO_3 ratio (samples M1.5–M7.0; Figure 2a–e) or applied reaction temperature T_R (samples M160–M240; Figure 2f–j).

Interestingly, for M7.0 (Figure 2e), produced with an excess of TU precursor, the nanosheets were found to aggregate into a flower-like or spherule-like morphology. The average nanosheet thickness of samples M4.5–M7 was found to be slightly higher (M4.5–M7: 11–13 nm; Figure S3e,f), when compared to those synthesized with lower TU/MoO_3 ratios (M1.5–M3.5: 7–9 nm; Figure S3b–d). The reaction temperature T_R seems to affect the morphology. Samples synthesized at low T_R (M160 and M180) exhibited structures with no well-defined 3D-branched architecture (Figure 2f,g, respectively), most probably because of insufficient energy. In contrast, at higher temperatures (samples M200–M240), the edges of nanosheets became sharper, indicating increased crystallization (Figure 2h–j). The growth mechanism for the formation of 3D self-assembled nanostructures is believed to be initiated by nucleation of an amorphous MoS_3 intermediate state, formed in the solution (described by eq 3) and subsequent outward growth of the crystalline MoS_2 nanosheets via a reduction process, where TU acted as a reducing agent.[26,35]

2.2.2. Elemental Mapping: SEM Energy-Dispersive X-ray (SEM-EDX). Energy-dispersive X-ray (EDX) microanalysis in the form of elemental mapping analysis and line scan-EDX profile (Figure S4a,b) confirmed the homogeneous distribution of Mo, S, and O elements over the hydrothermally synthesized nanosheets, indicating the successful formation of MoS_2/MoO_3. A considerably intense signal of the O element suggested the presence of oxide phases.

2.2.3. Crystallinity and Phase Identification: XRD Study. The crystallinity and phase identification of the hydrothermally synthesized MoS_2/MoO_3 nanosheets were further investigated by X-ray diffraction (XRD) analysis (Figure S5). X-ray diffraction patterns of hydrothermally synthesized samples at various TU/MoO_3 ratios (Figure S5a) and reaction temperatures T_R (Figure S5b) demonstrated a few peaks at 2θ angles of ~14, ~32, ~40, and ~57°, which originate from (002), (101/100), (103), and (110) planes, respectively, of the hexagonal structure of 2H-MoS_2 [JCPDS card no: 01-073-1508; space group $P6_3/mnc$]. The overall broadening and low-intensity peaks are indicative of short structural coherence length and suggest the presence of nanosized domains of mixed crystalline phases within the basal plane.[36,37] It should be noted that the XRD measurements were conducted in dry samples, where only fine differences can distinguish the predominance of the metallic over the semiconducting phase.[11,19,38] This is in contrast to XRD measurements performed on wet samples, where large shifts of the (002) peak position to lower angles could divulge straightway the transformation of 2H to 1T phase.[22,39] With the increase in the TU/MoO_3 ratio (Figure S5a), from 2.5 to 7, the (002) peak shifted to higher angles (from 13.45 to 14.04°), indicating a reduced interlayer spacing and progressive transformation of 1T to 2H phase. At the highest TU/MoO_3 ratio, M7.0 demonstrated well-defined (101/100) and (103) peaks, characteristic of the 2H-MoS_2-rich phase.

It is noteworthy that the XRD peaks in Figure S5 became significantly broadened with decreasing reaction temperature, suggesting a declined crystallinity. Among them, M160 was highly disordered since only a broad peak at ~35° could be observed. With increasing T_R to 180 °C, new broad peaks appeared; however, the (002) peak was still absent. With further increase in T_R, all peaks progressively sharpened, suggesting enhanced crystallinity and predominance of the 2H phase at temperatures of 220 and 240 °C (samples M220 and M240 in Figure S5b). The results are also in agreement with SEM observations, which revealed nanosheets with sharp well-defined edges at increased reaction temperatures, suggesting higher crystallinity in the synthesized products.

Taking into account the most intense (002) peak, the estimated interlayer *d*-spacing of the hydrothermally synthesized samples was found to be close (~0.625 nm for M7.0 and M240) or slightly larger (~0.66 nm for M2.5 and M200) to that of bulk MoS_2 (~0.615 nm).[40] Apparently, in the reported literature, the increment in the interlayer spacing is much larger and has often been attributed to the intercalation of ammonia or ammonium ions (NH_4^+) into the adjacent MoS_2 layers.[41,42] However, in our synthesis method, the intercalation of NH_3 or NH_4^+ could not be evidenced by the appearance of any distinctive peaks in the N 1s spectra of the samples (Figure S6).

The coexistence of 1T/2H-MoS_2 and MoO_3 phases in M2.5 was confirmed by Raman spectroscopy (λ_{ex} = 632.8 nm; Figure S7). Peaks observed at 376.4 and 404.1 cm^{-1} correspond to

https://dx.doi.org/10.1021/acsanm.0c03274
ACS Appl. Nano Mater. XXXX, XXX, XXX–XXX

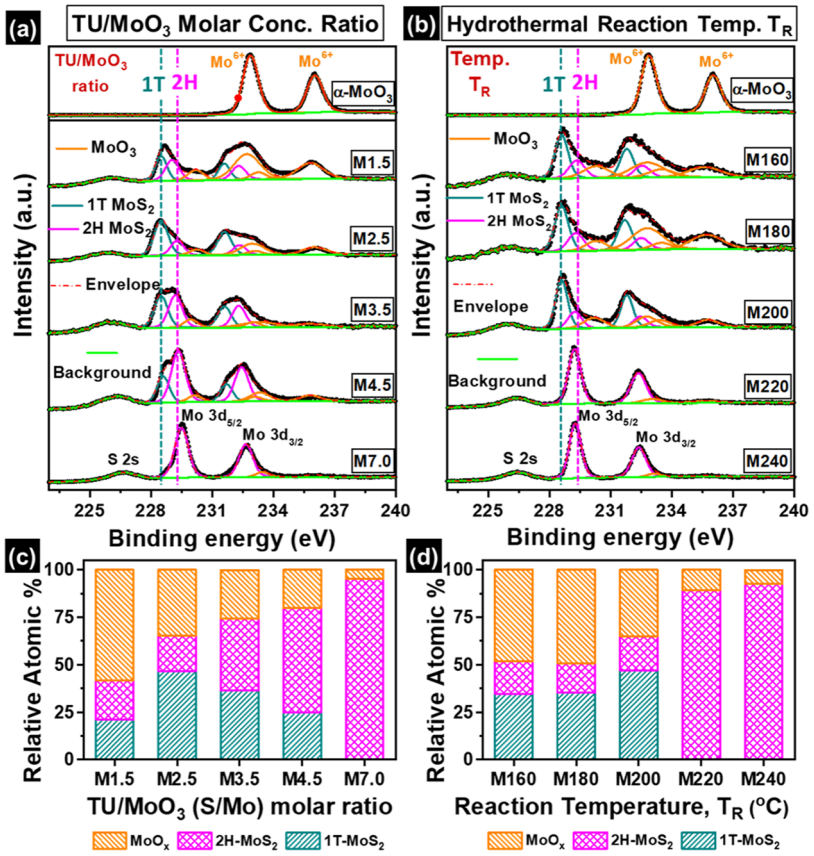

Figure 3. High-resolution XPS spectra of the Mo 3d core level for MoS_2/MoO_3 nanosheets synthesized with different (a) TU/MoO_3 molar ratios (M1.5−M7.0) and (b) reaction temperatures T_R (M160−M240). All spectra were deconvoluted to uncover 1T (teal) and 2H (magenta) phase contributions of MoS_2, Mo^{6+} oxide (orange), and intermediate Mo^{5+} (blue) oxidation states. (c, d) Relative contribution (%) of 2H-MoS_2, 1T-MoS_2, and Mo oxide phases (MoO_x) as a function of (c) TU/MoO_3 ratios and (d) T_R (derived from (a) and (b), respectively).

the well-known E^1_{2g} and A_{1g} bands of 2H-MoS_2 and are associated with the in-plane and out-of-plane Mo−S vibration modes, respectively. Peaks at 146.8 (J1), 236.5 (J2), and 335.8 cm^{-1} (J3), corresponding to the longitudinal acoustic phonon modes of the 1T phase, were also evident, confirming the coexistence of metallic and semiconducting phases.[1,43] The peak at 664 cm^{-1} corresponds to the characteristic B_{2g}/B_{3g} mode of MoO_3 associated with the asymmetrical stretching vibration of O−Mo−O bonds.[2,44]

2.2.4. Element, Phase Identification, and Quantification: XPS Study. X-ray photoelectron spectroscopy (XPS) provided validation and quantification of the mixed (1T/2H) MoS_2[17] as well as molybdenum oxide (denoted as MoO_x) phase formation. The XPS survey scans confirmed the presence of Mo, S, O, and C elements (Figure S8a,b). The intense O 1s signal in the XPS survey scan suggests the presence of oxide phases. Surface elemental composition analysis of the hydrothermally synthesized materials is tabulated in Table S2. A significant portion of the carbon content, most probably, originates from the decomposition of thiourea. The atomic concentration of oxygen in the samples was calculated from the area of O 1s core level spectra. A portion of this oxygen could be bonded to carbon atoms present on the surface of the samples and not to Mo. Deconvolution of Mo 3d peaks for both series of samples revealed the presence of MoO_x phases in addition to metallic (1T-MoS_2) and semiconducting (2H-MoS_2) MoS_2 phases. The estimated relative fractional percentages of different phases 1T-MoS_2/2H-MoS_2/MoO_x are presented in Table S3 and also in Figure 3c,d.

2.2.4.1. Mo/S Ratio. The Mo/S ratio in the samples was substoichiometric (M1.5: 1.44 ± 0.08; M2.5: 1.86 ± 0.01) at low TU contents (leading to an initial increase in pH from 7.2 to 7.6) due to insufficient S^{2-} production and partial conversion to Mo^{4+} (MoS_2). However, the excess of TU content led to a further increase in pH levels from 7.7 to 8.2 and was accompanied by a stoichiometric or slightly superstoichiometric Mo/S ratio (M3.5: 2.05 ± 0.07; M4.5: 1.99 ± 0.01; M7: 2.11 ± 0.05) due to adequate S^{2-} production and conversion efficiency of MoO_3 to MoS_2 (Table S2). Similarly, at low temperatures in the range of 160−200 °C, the Mo/S ratio in the samples was substoichiometric (M160: 1.63 ± 0.03; M180: 1.64 ± 0.08; M200: 1.865 ± 0.11) due to inefficient dissociation of TU (pH varied from 7.52 to 7.65). However, further increase in the reaction temperature led to an increase in pH from 7.7 to 7.8 and was accompanied by a stoichiometric or slightly superstoichiometric Mo/S ratio (M220: 1.99 ± 0.01; M240: 2.11 ± 0.05). The increase in pH is associated with increased ammonia levels, which indicate more efficient production of S^{2-} and conversion of MoO_3 to MoS_2. The substoichiometric S/Mo ratio observed in samples M1.5, M2.5, M160, M180, and M200 indicates the presence of S vacancies, which could be beneficial on HER-catalytic activity, as suggested by many studies.[10,11]

2.2.4.2. Phase Identification and Quantification. Phase quantification analysis was achieved via the high-resolution

https://dx.doi.org/10.1021/acsanm.0c03274
ACS Appl. Nano Mater. XXXX, XXX, XXX−XXX

XPS signals from Mo 3d and S 2p core levels, presented in Figures 3a,b and S8c,d, respectively. For all samples, the Mo 3d spectra exhibited doublet characteristics associated with Mo $3d_{5/2}$ and Mo $3d_{3/2}$ due to the spin−orbit coupling. Notably, these doublets distinctly shifted to lower energies for both M1.5−M7.0 (Figure 3a) and M160−M240 (Figure 3b) series, in comparison to those of α-MoO_3. Such red shift clearly confirms the formation of MoS_2 (Mo^{4+}) from the α-MoO_3 (Mo^{6+}) precursor.

The α-MoO_3 crystals exhibited doublets at 232.9 and 236.1 eV attributed to Mo^{6+} $3d_{5/2}$ and Mo^{6+} $3d_{3/2}$, respectively. In contrast, Mo 3d spectra of MoS_2/MoO_3 nanosheets exhibited multiple and asymmetric features, contributed from the Mo^{4+} of 2H and 1T phases of MoS_2 (presented by magenta- and teal-colored lines, respectively) and intermediate $Mo^{5+/4+}$ oxidation states of partially reduced MoO_3 (denoted as MoO_{3-x}).[16,45,46] The peaks located at 229.30 and 232.40 eV correspond to Mo^{4+} $3d_{5/2}$ and Mo^{4+} $3d_{3/2}$ characteristic peaks of the 2H phase (magenta lines), respectively, while those at 228.50 and 231.60 eV correspond to Mo^{4+} of the 1T phase (Table S3). The peaks originating from the 1T phase were found to be blue-shifted with respect to 2H phase peaks by around 0.8−0.9 eV, which agrees with the range of 0.5−1.0 eV, reported in the literature.[2,20,21,47] For quantification purposes, the estimated relative fractional percentages of different phases (Table S3), as derived from the respective Mo 3d spectra (Figure 3a,b), are depicted in Figure 3c,d for the TU/MoO_3 and T_R sequence of samples, respectively.

Among the M1.5−M7.0 series (Figure 3a,c), the M1.5 synthesized with the lowest TU concentration contained a very high contribution from MoO_3 (Mo^{6+}) or partially reduced (Mo^{5+}) molybdenum oxide phases (Figure 3a). The inadequate TU content led to insufficient S^{2-} production, resulting in an incomplete reduction of the Mo^{6+} (MoO_3) and its partial conversion to the Mo^{4+} (MoS_2).[48] Nevertheless, as the TU/MoO_3 ratio increased, the MoO_x phase contribution decreased significantly (Figure 3c); however, it did not disappear completely, even for the highest ratio (M7.0). Regarding the M160−M240 series (Figure 3b,d), a similar trend was observed with increasing reaction temperature. The contribution of the oxide phases was significant for the samples grown at low temperatures (≤200 °C). However, with further increase in T_R, the conversion rate of MoO_3 to MoS_2 was significantly improved, as evidenced from the significant suppression of the α-MoO_3 phase in Figure 3d. Notably, the M240 (synthesized at highest T_R) did not show complete removal of the Mo^{6+} or Mo^{5+} oxide phases. It should be noted that the presence of the MoO_3 phase could be related to unintentional oxidation from the exposure of the samples to the atmosphere,[49,50] even though caution was taken to avoid it.

Variations in the TU/MoO_3 ratio and T_R played a critical role in the yield of 2H and 1T phases. The initial increase in the TU/MoO_3 ratio from 1.5 to 2.5 resulted in the maximum contribution of 1T phase of 47% for sample M2.5 (Figure 3c). However, further increase in TU/MoO_3 caused a progressive dominance of the thermodynamically stable 2H phase over the metastable 1T phase, with M7.0 displaying almost pure 2H phase contribution (Figure 3c). The T_R series revealed improvement of the 1T phase content within the narrow T_R range of 160−200 °C, reaching a maximum (47.13%) at 200 °C (M200; Figure 3d). However, above 200 °C, the samples M220 and M240 were found to possess the pure 2H phase.

The S 2p XPS analysis (Figure S8c,d) was also taken into account to confirm the phase identification of MoS_2/MoO_3. Only the samples synthesized with the highest TU/MoO_3 ratio (M7.0) or those synthesized at higher T_R (M220 and M240) exhibited relatively symmetric doublets (S $2p_{3/2}$ and S $2p_{1/2}$) due to the spin−orbit coupling of S 2p orbitals. These three samples (M7.0, M220, M240) clearly showed pure 2H phase (magenta lines) contributions, around 162.2 eV (S $2p_{3/2}$) and 163.3 eV (S $2p_{1/2}$), arising from unsaturated and/or terminal S^{2-}.[51] The rest of the hydrothermally synthesized nanomaterials exhibited red-shifted asymmetric peaks due to the incorporation of the 1T phase into the MoS_2 matrix. This was reflected by the appearance of doublets at the lower binding energy side, located around 161.4 eV (S $2p_{3/2}$, teal line) and 162.6 eV (S $2p_{1/2}$, teal line), in addition to the respective 2H-MoS_2 phase (magenta lines).[2,15,20,52] Furthermore, an additional high binding energy contribution (blue line) was also observed around 163.1 eV (S $2p_{3/2}$, blue line) and 164.3 eV (S $2p_{1/2}$, blue line) for the samples synthesized with low TU/MoO_3 ratios or low T_R due to the intermediate oxidation state of $Mo^{4+/5+}$ bonded to the S atoms ($MoO_{3-x}S_y$).

2.2.4.3. Oxygen Content and Molybdenum Oxide Phases (MoO_x). In the TU/MoO_3 series, M1.5, M2.5, and M3.5 contained similar and relatively high oxygen atomic concentrations of 20.15 ± 0.84, 19.85 ± 0.37, and 19.07 ± 2.70 at. %, respectively, whereas M4.7 and M7 possessed reduced O levels of 14.44 ± 0.08 and 10.70 ± 1.73 at. %, respectively. However, a systematic decrease was observed on the overall relative fraction of the Mo oxide phases (calculated from the Mo 3d spectra) with increasing the TU/MoO_3 molar ratio, attaining levels of 58.2, 34.68, 25.54, 20.13, and 4.6% (Figure S9).

Thiourea served the dual purpose of sulfur source and reducing agent for the conversion of MoO_3 to MoS_2. Among M1.5−M7.0 series (Figure 3a,c), M1.5 synthesized with the lowest TU concentration contained a very high contribution from molybdenum oxide (MoO_x) phases, which consisted of MoO_3 (Mo^{6+}) and partially reduced (Mo^{5+}, Mo^{4+}) molybdenum oxide (Mo_2O_5 and MoO_2). This is because the inadequate TU content led to insufficient S^{2-} production and incomplete reduction of the Mo^{6+} (MoO_3) to the Mo^{4+} (MoS_2).[48] Nevertheless, as the TU/MoO_3 ratio increased, the MoO_x phase contribution decreased significantly (Figure 3c); however, it did not disappear completely, even for the highest ratio (M7.0).

Importantly, in the temperature series, the different temperatures control the crystallization process and incorporation of oxygen in the samples. With increasing the reaction temperature, the reaction process becomes more efficient (higher production of MoS_2), leading to reduced incorporation of oxygen, as can be seen in samples M220 and M240 (MoO_x level was reduced to 10.61 and 7.27%, respectively). In contrast, lower temperatures in the range of 160−200 °C promoted the incorporation of oxygen in the samples.

Importantly, in the temperature series, the different temperatures control the crystallization process in addition to the incorporation of oxygen in the samples. The degree of surface oxidation is higher for the lower-temperature, less well-crystallized, M160, M180, and M200 samples, when compared to that of higher-temperature (M220 and M240), higher-crystalline counterparts. M160, M180, and M200 contained a similar high oxygen atomic concentration of 19.29 ± 0.04, 21.90 ± 0.12, and 18.79 ± 1.23 at. %, respectively, whereas M220 and M240 possessed reduced O levels of 8.90 ± 0.08

https://dx.doi.org/10.1021/acsanm.0c03274
ACS Appl. Nano Mater. XXXX, XXX, XXX−XXX

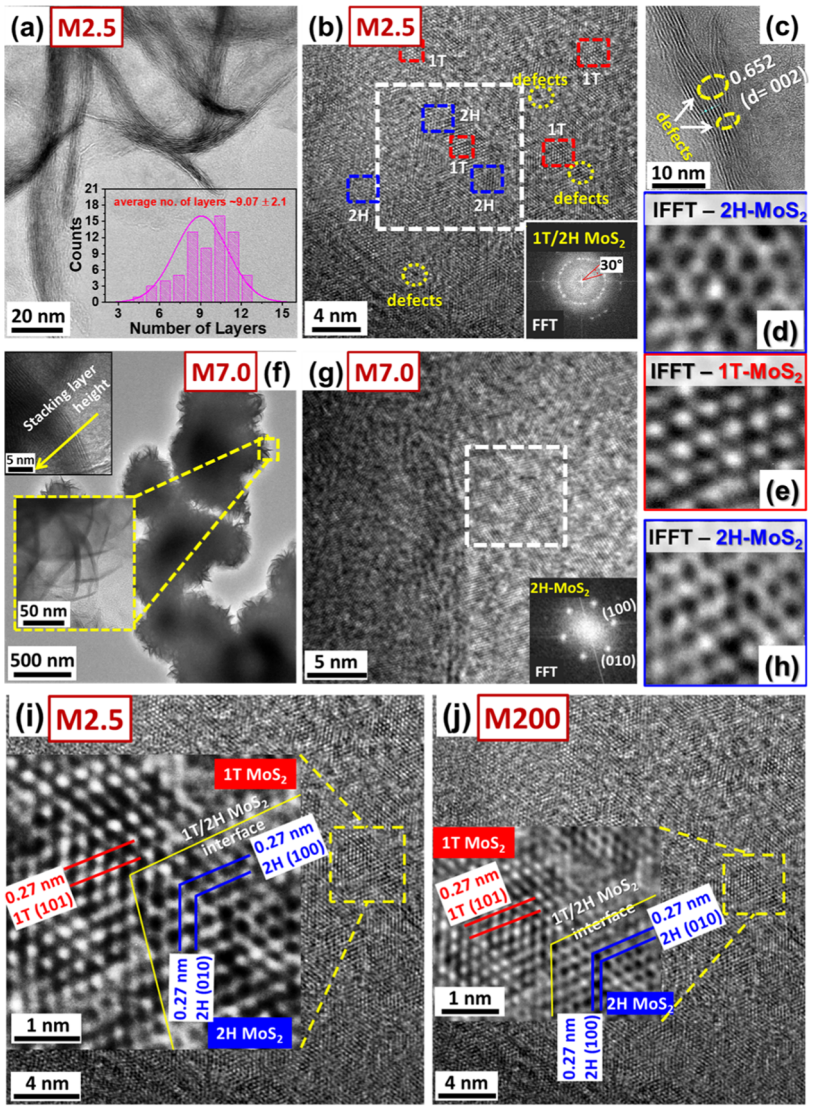

Figure 4. (a) Representative high-resolution TEM (HRTEM) image of the M2.5 sample displaying the layer stacking at the edge of nanosheets, with the estimated number of layer profile (inset, (a, c) lattice fringes). (b) HRTEM image of M2.5; the right-bottom inset represents the selected area electron diffraction (SAED) pattern collected from the region enclosed in a white rectangle on (b). (d, e) Representative inverse fast Fourier transformation (IFFT) images recorded from different regions enclosed in blue and red squares in (b), representing the (d) 2H-MoS_2 and (e) 1T-MoS_2 domains, respectively. Defect sites identified are enclosed in yellow circles in (b). M2.5 was selected as a representative 1T-MoS_2-rich phase. Comparative (f) low- and (g) high-magnification HRTEM images of M7.0 synthesized at the maximum TU precursor level; the respective SAED pattern (inset in (g)) and IFFT image (h) demonstrating typical 2H-MoS_2 domains. HRTEM images of (i) M2.5 and (j) M200 confirming the coexistence of metallic 1T-MoS_2 (on the left side of the yellow boundary labeled as "1T/2H-MoS_2 interface") and semiconducting 2H-MoS_2 phases (on the right side of the 1T/2H-MoS_2 interface) in nanoscale domains.

and 8.88 ± 1.23 at. %, respectively. A similar decreasing trend was observed on the overall relative fraction of Mo oxide phases with increasing reaction temperature, obtaining levels of 48.41, 49.28, 35.05, 10.61, and 7.27% (Figure S9). The lower MoO_x levels at higher temperatures are associated with more efficient dissociation of TU and conversion of MoO_3 to MoS_2. Importantly, in the temperature series, the different temperatures control the crystallization process in addition to the incorporation of oxygen in the samples.

2.2.5. Coexistence of 1T/2H-MoS_2 and 1T-MoS_2/MoO_3 Heterojunctions: HRTEM Study. The high-angle annular dark-field scanning transmission electron microscopy (HAADF-STEM) image of M2.5 and corresponding energy-dispersive X-ray (EDX) element mappings (Figure S10a) revealed the uniform distribution of Mo, S, and O elements in the sample, indicating the coexistence of sulfide and oxide phases, corroborating the findings by SEM-EDX (Figure S4), XPS (Figure 3c,d), and Raman analysis (Figure S7).

HRTEM images revealed transparent nanosheets with wrinkled morphology reflecting their ultrathin layered structure (M2.5 in Figures 4a and S10b; M200 in Figure S11a). Edge view images demonstrate that the nanosheets are approximately 5−10 nm thick, consisting of 7−11 layers (Figures 4a (inset),c, S10c, and S11a (inset)) and are thinning down to a couple of layers at the very end. It is noticed in Figure 4c (also Figures S10c and S11a (inset)) that the lattice fringes along the curled edges are discontinuous, providing additional edge defects, beneficial for HER. The interlayer spacing calculated from the line profile plots (Figure S10d) was found to be 0.653 nm, which corresponds to the (002) plane

https://dx.doi.org/10.1021/acsanm.0c03274
ACS Appl. Nano Mater. XXXX, XXX, XXX−XXX

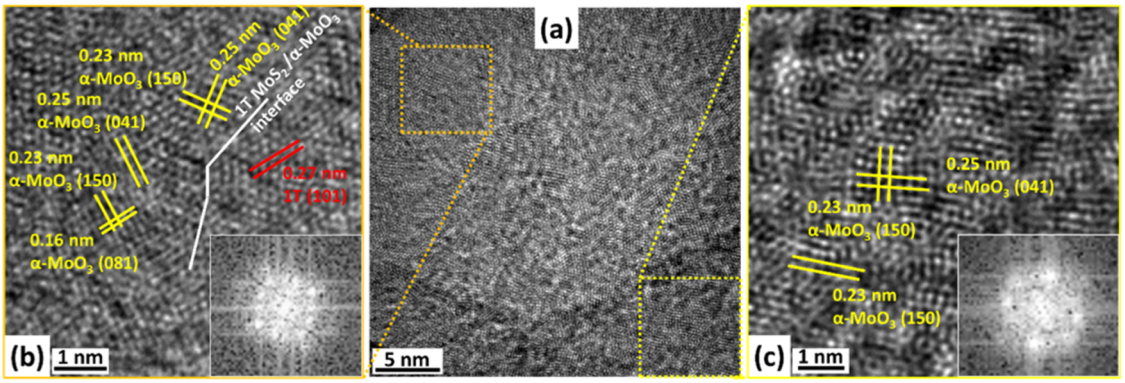

Figure 5. (a) HRTEM image of sample M2.5 with (b) and (c) showing zoomed-in areas marked by dotted squares. Lattice planes are labeled, especially those corresponding to α-MoO_3. The presence of the 1T-MoS_2/α-MoO_3 heterostructure is depicted in (b). Insets in (b) and (c) show SAED patterns corresponding to areas of (b) and (c).

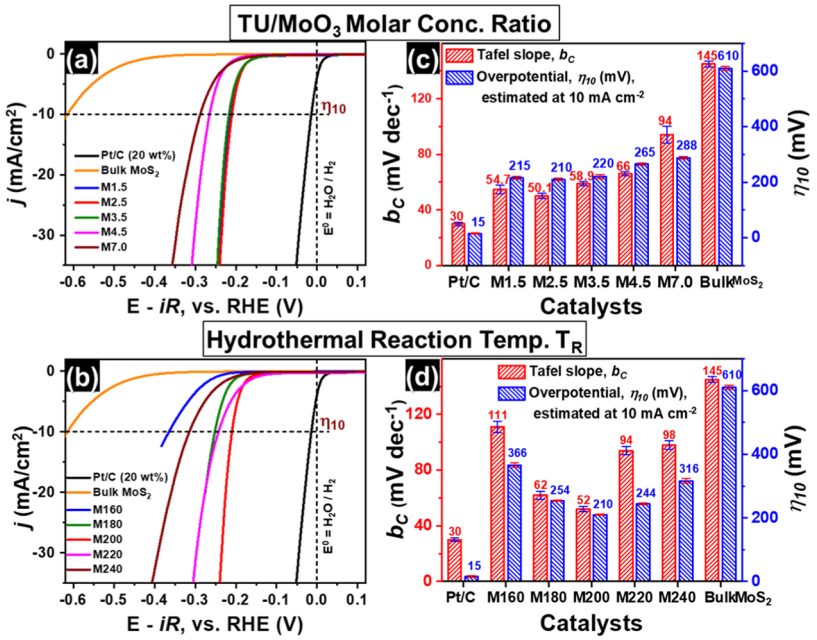

Figure 6. Electrocatalytic activity of (1T/2H) MoS_2/MoO_3 electrocatalysts for hydrogen evolution reaction (HER) in an aqueous acidic medium (0.5 M H_2SO_4): (a, b) LSV plots (*iR*-corrected) of electrocatalysts synthesized with different (a) TU/MoO_3 ratios (M1.5−M7.0) and (b) reaction temperatures T_R (M160−M240) at a potential scan rate of 5 mV/s, with a rotating disk electrode (RDE) rotation speed of 1600 rpm. (c, d) Comparison of HER activities in terms of the cathodic Tafel slope (b_C) and overpotential (η_{10}, estimated at 10 mA/cm^2) for (c) M1.5−M7.0 and (d) M160−M240 electrocatalysts. Respective data measured at the commercial MoS_2 powder and Pt/C (20 wt %) electrocatalysts are presented for comparison. Catalyst mass loading of ≈ 0.283 mg/cm^2.

of MoS_2 (Figure 4c), being in agreement with XRD results (Figure S5).

In comparison, the M7.0 sample synthesized with an excess of TU precursor displayed a self-assembled flower-like morphology (Figure 4f) composed of multiple petals emanating from a central region in agreement with the SEM findings (Figure 2e). The petal edges appear curled and ultrathin in nature (Figure 4f and its top inset). At a high-temperature synthesis of 240 °C, lattice fringes along the edges displayed fewer defects (Figure 4f), suggesting increased crystallinity, in agreement with XRD results.

Validation of the successful formation of the 1T/2H phase in the basal plane was provided through high-resolution transmission electron microscopy (HRTEM) on M2.5 (Figure 4b) and M200 (Figure S11b) samples. Both samples were produced under similar conditions (differ only in the reaction time; M2.5: 24 h and M200: 18 h) and according to XPS analysis exhibited the maximum 1T phase contribution of ∼47 % (Figure 3c,d). HRTEM analysis of M2.5 and M200 (Figures 4b and S11b, respectively) confirmed the coexistence of nanoscale domains (3−5 nm) of metallic 1T (indicated by red squares) and semiconducting 2H phases (indicated by blue squares) on the basal planes. Inverse fast Fourier transformation (IFFT) micrographs of the region indicated by the red square revealed trigonal lattices with octahedral coordination of Mo atoms confirming the 1T-MoS_2 phase formation (Figures 4e and S11c). IFFT images (Figures 4d and S9d) of regions indicated by blue squares displayed a honeycomb lattice with the trigonal prismatic coordination of Mo atoms consistent with the 2H-MoS_2 phase.[8,19] Also, the SAED pattern (collected on the white rectangle areas of Figures 4b and S11b) showed two sets of diffraction spots, one set of

https://dx.doi.org/10.1021/acsanm.0c03274
ACS Appl. Nano Mater. XXXX, XXX, XXX−XXX

spots with a sixfold (hexagonal) symmetry rotated at 30° relative to the second set of spots (insets of Figures 4b and S11b), indicating the formation of two different phases.[18] Further evidence was obtained from Figure 4i (M2.5),4j (M200) that confirmed the coexistence of 1T-MoS_2 and 2H-MoS_2 (with a lattice spacing of 0.27 nm corresponding to the (100) plane) domains on the basal plane and the formation of crystalline defects at the 1T/2H boundary (marked by yellow lines in the figures). Furthermore, several defect sites were identified on the basal planes, marked by yellow circles in Figures 4b and S11b.

In contrast, samples synthesized with excess TU precursor (M7.0) or at highest T_R (M240) displayed the almost pure 2H phase (Figure 3c,d), clearly demonstrated by SAED patterns of a single set of sharp diffraction spots with sixfold hexagonal symmetry (insets of Figures 4g and S11f) or by IFFT images of only 2H-MoS_2 domains (Figures 4h and S11g).

Importantly, the presence of α-MoO_3 nanodomains and 1T-MoS_2/MoO_3 heterojunctions in sample M2.5 was confirmed by HRTEM images presented in Figure 5. As shown in Figure 5b,c, the interplanar distances of 0.27, 0.25, 0.23, and 0.16 nm were identified, corresponding to 1T-MoS_2 (101), α-MoO_3 (041), α-MoO_3 (150), and α-MoO_3 (081) planes, respectively, confirming the coexistence of 1T-MoS_2 and MoO_3. The SAED patterns presented in the insets match the orthorhombic lattice of α-MoO_3.

In summary, these aforementioned XPS, Raman, and HRTEM results collectively demonstrate the successful formation of MoS_2/MoO_3 hybrid incorporating 1T/2H-MoS_2 and 1T-MoS_2/MoO_3 heterostructures as well as MoO_3 nanodomains.

2.3. Electrocatalytic Activity for Hydrogen Evolution Reaction (HER). *2.3.1. HER Activity of MoS_2/MoO_3 Electrocatalysts.* The HER-catalytic performance of MoS_2/MoO_3 electrocatalysts obtained at various precursor ratios and reaction temperatures T_R is demonstrated in Figure 6. Linear sweep voltammograms (LSVs; Figure 6a,b) were measured as a function of potential with respect to the reversible hydrogen electrode (RHE) in an aqueous acidic medium (0.5 M H_2SO_4). For comparison, the HER activities of commercial Pt/C (20 wt %) and commercial bulk 2H-MoS_2 powder are also presented in Figure 6. All working electrodes (WEs), including Pt/C and bulk MoS_2-based catalysts, were prepared by drop-casting the respective catalyst ink (3 mg/mL in DMF solvent) on a commercial glassy carbon electrode (GCE) maintaining the final catalyst mass loading around 0.283 mg/cm^2 (details in the Supporting Information, under the Experimental Details section, Electrochemical Studies subsection).

As revealed from the *iR*-corrected polarization curves (LSV plots), the hydrothermally synthesized MoS_2/MoO_3 hybrids exhibited HER performances superior to bulk 2H-MoS_2, though still inferior to the Pt/C electrocatalyst. Detailed analysis of the LSV data, in terms of the onset potential (V_{OC}) and overpotential (η_{10}) required to get a current density of 10 mA/cm^2, disclosed that the rich 1T phase MoS_2/MoO_3 nanosheets performed much better than their 2H-rich counterparts (Table S4). M2.5 (Figure 6a) and M200 (Figure 6b) possessing the maximum metallic 1T phase contribution of ~47 % attained the lowest V_{OC} (around −0.123 V vs RHE) and the highest current densities (achieving 10 mA/cm^2 at η_{10} of 210 mV) (Figure 6c,d and Table S4).

It is reminded that the deconvolution of XPS peaks for both series of samples revealed the presence of Mo oxide phases (MoO_x), in addition to 1T/2H-MoS_2. The estimated relative fractional percentages of different phases 1T-MoS_2/2H-MoS_2/MoO_x are presented in Table S3 and also in Figure 3c,d. Concerning the effect of MoO_x phases in the HER performance, it is well known that MoO_3 (with Mo^{6+} states) is not particularly active toward HER,[53,54] mainly due to its low conductivity. However, Mo^{5+} states give rise to substoichiometric MoO_{3-x}, with metallic conductivity due to the presence of oxygen vacancies, which are regarded as active sites for HER. Recently, an increasing number of researchers reported an enhancement of the HER electrocatalytic activity on MoS_2/MoO_3 or WS_2/WO_3, which was attributed to the H intercalation in metal oxide layers (MoO_3, WO_3) and subsequent spillover to metal disulfides.[24,55,56] Additionally, according to the density functional theory (DFT) calculations, the coupling of MoO_3 with 1T-MoS_2 interfaces induces a slight out-of-plane distortion on the 1T-MoS_2 phase, leading to significantly lower hydrogen adsorption free-energy (ΔG_H*) values, favorable for the HER reaction.[24] Our HRTEM images in sample M2.5 (Figure 5) revealed the presence of 1T-MoS_2/MoO_3 heterojunctions, suggesting their beneficial role on HER.

2.3.1.1. HER LSV Performance for TU/MoO_3 Series. LSVs for M1.5, M2.5, and M3.5, appear similar (Figure 6a); however, a closer look at their electrochemical characteristics reveals that M2.5 exhibits the best electrocatalytic behavior among the three samples, followed by M1.5 and M3.5. It is worth noticing that the behavior of these lower TU/MoO_3 ratio samples is markedly better than those at higher ratios (M4.5 and M7). To explain the relatively similar HER performance of samples M1.5, M2.5, and M3.5 compared to those of M4.5 and M7, one should take into account the following points.

First, the Mo/S ratio in M1.5, M2.5, and M3.5 increases with the TU/MoO_3 molar ratio, obtaining values of 1.44, 1.86, and 2.05, respectively. The substoichiometric values for M1.5 and M2.5 indicate the presence of sulfur vacancies, which could have a positive impact on the HER performance. Second, the yield of the 2H semiconducting phase is similar to that for M1.5 and M2.5 (20.8 and 18.65%, respectively); however, it is larger for M3.5 (27.9%). In M4.5 and M7, the 2H phase is dominant, with levels reaching 55.13 and 95.25%, respectively. Third, the 1T phase has a bell shape, reaching a maximum for M2.5 (46.66%) and has minima from either side at M1.5 (21.0%) and M4.5 (24.73%), with M7 been depleted of any metallic phase (0%). Fourth, the yield (%) of Mo oxide phases is decreasing with the TU/MoO_3 molar ratio, obtaining levels of 58.2, 34.68, and 25.54% for M1.5, M2.5, and M3.5, respectively. Among these Mo oxide phases, Mo^{5+} states give rise to substoichiometric MoO_{3-x}, with metallic conductivity and the presence of oxygen vacancies, which are regarded as active sites for HER. Importantly, the presence of either 2H-MoS_2/MoO_3 or 1T-MoS_2/MoO_3 heterojunctions can also enhance the HER via various mechanisms, as stated previously.

So, there are a number of competitive components, such as the 1T-MoS_2 metallic phase, S vacancies in MoS_2 and oxygen vacancies in MoO_3, and heterojunctions between 1T-MoS_2 and MoO_3, all of which contribute positively to HER, vs semiconducting MoS_2, and insulating MoO_3 phases with an adverse effect toward HER. The contribution, positive or negative, of all of these components gives rise to the relatively similar performance for M1.5, M2.5, and M3.5 compared to that for M4.5 and M7.

https://dx.doi.org/10.1021/acsanm.0c03274
ACS Appl. Nano Mater. XXXX, XXX, XXX−XXX

Besides, the catalytic activity could be correlated to the oxygen content of the heterophase MoS_2/MoO_3 nanosheets (Figure S12). It is noted that the oxygen atomic % (at. %) at low TU/MoO_3 molar ratios (M1.5, M2.5, and M3.5) was relatively high, obtaining levels of about 19.7 ± 0.6 at. %, whereas, at higher molar ratios (M4.5, M7), the oxygen atomic concentration was decreased to levels of 14.5 and 10.7 at. %, respectively. The boosted HER response and comparable oxygen concentration for all three M1.5, M2.5, and M3.5 samples reveal that the oxygen has an unambiguously positive effect on improving the activity of MoS_2/MoO_3, mainly by increasing the electrical conductivity, as confirmed by EIS results (Figure S16). Although the results are in line with the earlier experimental and theoretical studies, which indicate that oxygen incorporation can effectively regulate the electronic structure of MoS_2 leading to enhanced intrinsic conductivity, highly beneficial for HER, the oxygen concentration levels in the present study are much higher than those reported (2−3.4 at. %) earlier.[57]

2.3.1.2. HER LSV Performance for the Temperature Series. In the temperature series, the best HER performance was observed for M200 followed by M180, M220, M240, and M160. M160 and M240, with considerably different fractions of phases (1T-MoS_2/2H-MoS_2/MoO_x for M160 = 34.73:17.07:48.41 and M240 = 0:92.53:7.27), exhibited the poorest HER activities among the hydrothermally synthesized electrocatalysts (Figure 6c,d and Table S4).

It is worth noting that M160 and M180 even though they have similar relative fractions of 1T-MoS_2/2H-MoS_2/MoO_x (M160 = 34.73:17.07:48.41, M180 = 35.18:15.55:49.28) and also similar S/Mo ratios (1.63 ± 0.03, 1.64 ± 0.08; 1.86 ± 0.11) exhibit dramatically different HER response.

Although one could argue that highly disordered structures could offer more active sites for HER the electrical conductivity is another important factor that should also be taken into consideration. Electrochemical impedance spectroscopy (EIS) (Figure S16) revealed that M160 had a considerably higher charge-transfer resistance value (2108 Ω) compared to M180 and M200 (169, 42.1 Ω), indicating that electron transport was significantly hindered. Hence, it can be concluded that the considerably reduced HER activity of M160 is associated with the reduced electrical conductivity in the sample.

It is worth noting that, since the reaction temperature can significantly affect the reduction kinetics of the precursors, the oxygen level in the produced electrocatalysts changed drastically with temperature. Our experimental results indicate that slow reduction kinetics at low reaction temperatures (M160, M180, M200) led to relatively high oxygen levels of about 20.0 ± 1.7 at. %, whereas at higher temperatures (M220, M240), oxygen was decreased to levels of ∼8.9 at. % due to the efficient transformation of MoO_3 to MoS_2 (Figure S12). Although one could argue that high oxygen levels would contribute positively to HER by increasing the electrical conductivity, this is not the case for the M160 sample. Both M160 and M240 with considerable diverse oxygen levels (19.29 ± 0.04 and 8.88 ± 1.23 at. %) exhibited poor HER activity due to reduced electrical transport. On the other hand, M160 and M200 with relatively similar oxygen levels displayed distinctly different HER activities. These contradictions can be lifted bearing in mind the different degree of crystallinity between M160 and M240. The high degree of disorder in M160 hinders electron transport, even though it incorporates a large amount of oxygen. As a result, crystallinity is an important factor that should be taken into account, when comparing samples with either similar or diverse oxygen contents.

2.3.1.3. Tafel Analysis. The Tafel analysis of the polarization curves, at low cathodic currents (Figure S13a,b; η (V) vs log(j) (mA/cm^2)), provided two important figures of merit in HER electrocatalysis, namely, the cathodic Tafel slope (b_C) and exchange current density (j_0). Especially, b_C is a valuable indicator to probe the rate-determining step of H_2 evolution reaction (details in the Supporting Information) and could be estimated directly from the linear fitting of the Tafel plots using eq S3. The exchange current density (j_0) was obtained by the intercept of the Tafel plot and increases with a decrease in the Tafel slope, indicating a faster reaction rate. A low value of the Tafel slope is indicative of fast kinetics since this is attested by a reduced overpotential required to achieve appreciable current density.

Tafel slope decreased from ∼100 mV/dec for the pure 2H (M7.0, M220, and M240) or highly disordered/poorly conductive (M160) electrocatalysts to ∼50 mV/dec for the highly conductive 1T-rich phase (M2.5 and M200) with an excess of active sites (Figure S13 and Table S4). Additionally, the increased exchange current density (j_0 ∼ 1.3 μA/cm^2) and reduced V_{OC} reflect the improved catalytic performance (Table S4) for the latter. These findings indicate that for conductive, 1T-rich electrocatalysts with a surplus of defects, hydrogen desorption is the rate-determining step and HER proceeds through a combination of Volmer−Heyrovsky and Volmer−Tafel mechanisms (see the Supporting Information on the HER mechanisms), whereas hydrogen adsorption (Volmer reaction) is the rate-determining step in the pure 2H phase or poorly conductive electrocatalysts.

The HER performance of the rich 1T phase MoS_2/MoO_3 nanocomposite presented in this work compares favorably to MoS_2 nanoflowers,[22] oxygen-incorporated MoS_2,[58] defect-rich MoS_2,[36] core−shell MoO_3−MoS_2 nanowires,[59] phase engineering 1T/2H-MoS_2,[21] 1T-MoS_2 nanopetals,[7] and heterogeneous 1T/2H-MoS_2 nanosheets[19] (summarized in Table S5) reported previously.

2.3.2. Electrochemically Active Surface Area (ECSA). The enhancement in the active site density for highly conductive 1T-rich catalysts (M2.5 and/or M200) was further confirmed by estimating their effective electrochemically active surface area (ECSA), using eq S6. The ECSA values were derived from the respective double-layer capacitance (C_{dl}), using eq S6, via conducting cyclic voltammograms (CVs) in a non-faradic potential region at various scan rates (Figure S14A−C), following the McCrory et al.'s methodology.[60,61] M2.5 and M200 exhibited the largest C_{dl} (1.27−1.45 mF) and hence ECSA values (21.2−24.2 cm^2) among the studied catalysts (Table S4). These maximum values confirm the presence of high-density catalytic active sites. Similarly, the roughness factor (RF) values (Table S4), estimated by eq S6, were also found to be the highest. Table S4 also revealed a dramatic decrease in C_{dl}, hence ECSA with an increase in the 2H phase, indicating a substantial reduction in the active site density, especially for M7.0 (C_{dl} ≈ 0.44 mF, ECSA ≈ 7.4 cm^2, RF ≈ 104.5), M220 (C_{dl} ≈ 0.25 mF, ECSA ≈ 4.1 cm^2, RF ≈ 58.6), and M240 (C_{dl} ≈ 0.05 mF, ECSA ≈ 0.8 cm^2, RF ≈ 10.7), which showed almost pure 2H phase. As expected, relatively low C_{dl} and ECSA values were also observed for the highly disordered low-conductivity M160 hybrid.

https://dx.doi.org/10.1021/acsanm.0c03274
ACS Appl. Nano Mater. XXXX, XXX, XXX−XXX

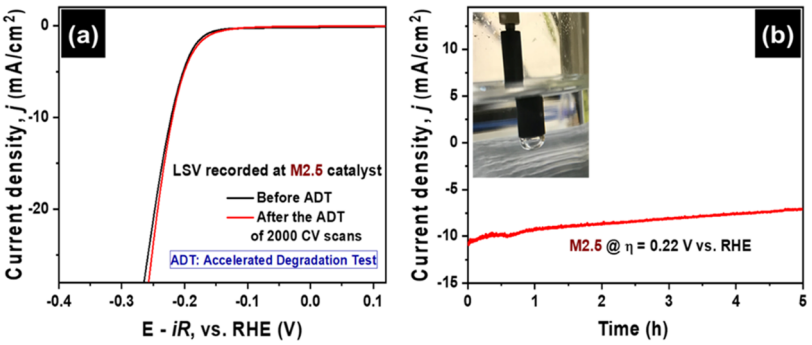

Figure 7. Long-term stability and durability tests in 0.5 M H_2SO_4 of the M2.5 electrocatalyst with the rich 1T phase. (a) Polarization curves (LSV plots) recorded before and after the accelerated degradation test (ADT, conducted continuous CV scans at a rate of 100 mV/s up to 2000 cycles between +0.41 and −0.29 V vs RHE). (b) Chronoamperogram obtained at a static overpotential of −0.22 V vs RHE. The inset displays the H_2 gas bubble formation at the electrode−electrolyte interface during measurement. A graphite rod (Goodfellow, U.K.) was used as the counter electrode (CE) for all of the stability and durability tests.

2.3.3. Turnover Frequency (TOF) for TU/MoO_3 Series. The intrinsic activity of the electrocatalysts was studied using the turnover frequency (TOF), which represents the number of hydrogen molecules produced per second per active site. In our calculations, we estimated the number of active sites, assuming that the sulfur atoms are the only active sites (Supporting Information provides details on the calculation of the TOF values).[62]

Figure S15 shows the TOF values of electrocatalysts obtained at various TU/MoO_3 ratios and reaction temperatures T_R, plotted against the applied potential. There is an overall general agreement in the trends observed between the HER LSVs and TOF curves. In the TU/MoO_3 ratio series, it is evident that for the 2H-rich samples (M4.5 and M7; see Figure 3c), produced at the higher TU/MoO_3 ratios, the turnover frequencies are more than an order of magnitude lower than those of samples produced under lower ratios (M1.5, M2.5, M3.5). These three samples have a lower content of 2H phase (20.8, 18.7, and 37.9%, respectively) compared to those of M4.5 (55.1%) and M7 (95.3%). M1.5 and M2.5 have a Mo/S ratio lower than 2, which indicates the presence of sulfur vacancies as discussed earlier. It should be noted that M1.5 has a large content of molybdenum oxide phases (58.2%) of which 11.8% (Mo_2O_5) could be electroactive. As a result, the presence of the metallic phase, along with sulfur vacancies and substoichiometric MoO_{3-x}, contributes positively to the HER activity.

2.3.4. Turnover Frequency for Temperature Series. In the temperature series, the TOFs for M160 and M240 are more than an order of magnitude lower than those of samples produced at intermediate temperatures (M180, M200, M220), as shown in Figure S15b. The inferior behavior for M240 is associated with the highest level of the semiconducting phase (96%). M160 synthesized at the lowest reaction temperature possessed a highly disordered structure, which considerably hindered electronic transport, as confirmed by electrochemical impedance studies (Figure S16). At a potential of −0.2 V (vs RHE), the TOF for M200 with the highest metallic phase and the presence of 1T-MoS_2/MoO_3 heterojunctions was estimated as 0.25 H_2 s^{-1}, which is approximately 2 orders of magnitude higher than those of the 2H-rich, M240 and highly disordered M160 samples with TOFs of about 0.0009 H_2 s^{-1} (Table S4). It should be noted that such calculations incorporate large errors as it was assumed that the S sites are the only active sites in the samples.

2.3.5. Electrochemical Impedance Spectroscopy. Further investigation with the AC electrochemical impedance spectroscopy (EIS), for the TU/MoO_3 series shown in Figure S16a, revealed that M1.5, M2.5, and M3.5 exhibited the lowest R_{ct} along with the largest ECSA values (Table S4), which is consistent with the polarization measurements and respective Tafel and TOF analysis. In contrast, the 2H-rich M4.5 and M7 samples displayed considerably increased R_{ct} values.

In the temperature series, the highly disordered M160 and 2H-rich M240 samples exhibited the highest R_{ct} values (Figure S16b), along with the lowest ECSA values, which is in agreement with the rest of the electrochemical characteristics of the samples.

2.3.6. HER in Alkaline Electrolytes. HER in alkaline electrolytes is important in terms of the popular water−alkali and chlor−alkali electrolyses.[63,64] However, MoS_2-based electrocatalysts exhibit limited response in basic solutions due to the higher activation energy for water dissociation and the difficulty of generated intermediates (OH^-) to desorb from the catalyst surface. M2.5 showed higher electrocatalytic activity for the evolution of H_2 in acidic solution (0.5 M H_2SO_4) than in alkaline (1 M KOH). The overpotentials required to drive hydrogen evolution at −10 mA cm^{-2} of current density were −0.293 and −0.210 V when in contact with 1.0 M KOH and 0.5 M H_2SO_4, respectively. The corresponding Tafel slopes were 115 ± 1 mV/dec for the basic and 50 ± 2 mV/dec for the acidic electrolytes (Figure S17).

2.3.7. Stability and Durability of HER Electrocatalysts. To establish the potential of any catalyst, besides its electrocatalytic activity, its long-term cycling stability is another key criterion for practical applications. Here, the M2.5 was selected for testing since it exhibited the best HER performance. Initially, the M2.5 catalyst was subjected to accelerated degradation test (ADT) by performing continuous CV scans at a potential scan rate of 100 mV/s in 0.5 M H_2SO_4. Figure 7a displays the LSV curves recorded before and after 2000 cycles of continuous CV scans. The negligible difference between the LSV curves indicates that the hydrothermally synthesized MoS_2/MoO_3 catalyst remained remarkably stable under the long-term electrochemical process.

Here, it is important to mention that, for all stability and durability tests, a commercially purchased graphite rod (Goodfellow, U.K.) was used as the counter electrode (CE). Use of a Pt wire as CE in ADT experiments of 1000 continuous CV cycles confirmed unwanted Pt electro-

https://dx.doi.org/10.1021/acsanm.0c03274
ACS Appl. Nano Mater. XXXX, XXX, XXX−XXX

deposition on WE, which led to a substantial enhancement in the HER activity (Figure S18a), obscuring the true contribution of the hydrothermally synthesized MoS_2/MoO_3 electrocatalyst.[31] As a result, we avoided the use of a Pt wire as CE in HER for any long-term stability studies. However, when the HER performance of a hydrothermally synthesized MoS_2/MoO_3 electrocatalyst was checked using both Pt wire and graphite rod as CEs, in two independent LSV runs, no difference could be seen in the polarization curves (Figure S18b).

Another durability test was also conducted on sample M2.5 by performing constant potential amperometry (CPA) at a fixed overpotential of 0.220 V vs RHE for 5 h. The resulting chronoamperogram shown in Figure 7b revealed decay in the HER current density, retaining 66% of the initial value after a 5 h CPA test (Figure S19). Initially, the sample exhibited intensive formation and release of small H_2 bubbles on the electrode surface. At later stages, the bubbles grew larger, before detaching from the surface (inset in Figure 7b). Adherence of bubbles to the electrode surface hindered the effective contact between the electrolyte and electrocatalyst, resulting in ohmic losses and reduction of reaction efficiency. Effective removal of bubbles from the electrode surface represents a critical issue for high-performance electrocatalysis. Rotating the electrode during the stability measurements is a popular approach[65] for promoting bubble release; however, it has limited industrial applications since static working conditions are most favorable. Our stability measurements were contacted under static conditions, and longer tests up to 10 h led to the formation of a large bubble permanently attached to the electrode surface, blocking electrolyte diffusion, resulting in a severely compromised performance (maintaining 54% of the current density; Figure S19); bursting of the bubble resulted in the mechanical delamination of the electrocatalyst from the electrode's surface. Future efforts will be focused on increasing the superaerophobicity of the nanosheets with a view of decreasing the adhesion force between the bubbles and electrocatalyst and hence accelerate the bubble departure.[66,67]

3. CONCLUSIONS

This is the first time that a detailed material synthesis/structure/catalytic property relationship triangle of self-assembled MoS_2/MoO_3 nanosheets, produced by a one-step hydrothermal route using α-MoO_3 and thiourea (TU) as Mo and S precursors, is reported. A complete study of the atomic structure, chemical bonding, and crystalline quality shed light on the evolution of 1T/2H-MoS_2 and Mo oxide phases by systematically varying the α-MoO_3/thiourea (TU) precursor ratio and reaction temperature T_R and uncovered how the modulation of their electronic structure relates to the catalytic activity for hydrogen evolution reaction. The study allowed the identification of a kinetically controlled regime of hydrothermal synthesis that enabled nucleation and growth of a 3D network of branched few-layered nanosheets consisting of 1T/2H-MoS_2 and 1T-MoS_2/MoO_3 nanoscale heterostructures, with a high yield of metallic contribution and defects in a reproducible manner. We found that 3D networks of ultrathin nanosheets synthesized at a TU/MoO_3 ratio of 2.5 and a T_R of 200 °C exhibited the highest metallic 1T phase contribution of ~47 %, which was directly connected to the best HER performance, reflected by a small overpotential at 10 mA/cm^2 (η_{10}) of ~210 mV and a small Tafel slope of ~50 mV/dec in 0.5 M H_2SO_4. In addition to the high metallic content emanating from the 1T phase, several other key factors were synergistically regulated and contributed to the HER performance. These include the presence of (i) 1T-MoS_2/MoO_3 heterostructures, which enhanced the charge transfer between 1T-MoS_2 and MoO_3 domains; (ii) abundance of sulfur vacancies in substoichiometric MoS_{2-x} and oxygen vacancies in substoichiometric MoO_{3-x}, edge sites at the ultrathin nanosheets (7−11 layers), and defects at the heterojunction between 1T- and 2H-MoS_2 interfaces, all of which act as active sites for HER. Overall, this work has established a controllable phase/disorder engineering approach in the 2D layer-structured TMD synthesis, opening a prospect for synergistic structural and electronic modulations for electrocatalytic applications. In addition, the work promoted the understanding of synthesis-structure-dependent catalytic relationships, providing new insights into designing efficient electrocatalysts via modulation of multiple phases, their interfaces, and incorporating different functional active sites into material systems.

4. EXPERIMENTAL DETAILS

4.1. Hydrothermal Synthesis of MoS_2/MoO_3 Nanosheets. The MoS_2/MoO_3 nanosheets were synthesized by a facile one-step hydrothermal reaction. The as-purchased molybdenum trioxide (α-MoO_3, 10 mM) was dissolved in 15 mL of Milli-Q water and magnetically stirred for 30 min. Then, thiourea (NH_2CSNH_2 or TU, 15−70 mM) was added as a sulfur source and reducing agent (dual role), and the solution was stirred for another 15 min. Finally, the above solution (65% capacity-filled water) was transferred into a 23 mL capacity Teflon-lined autoclave (Parr Instrument), which was positioned into a temperature-programmed electric oven. The temperature was increased to a desirable level (160−240 °C) at a ramping rate of 5 °C/min. After curing at the final reaction temperature for 24 h, the oven was switched off and allowed to cool naturally to room temperature. The obtained products were washed with DI water and anhydrous ethanol three times. The final product was collected by centrifugation at 10 000 rpm (Thermo Scientific, U.K.). The sediment was dried by a vacuum oven at 50 °C for 10 h and immediately used to perform the electrocatalytic studies. It is important to mention here that the samples were stored in a water medium prior to examining microstructural and electrochemical studies.

The as-proposed hydrothermal-based synthesis process was systematically optimized by tuning either the S/Mo molar ratio or the reaction temperature (T_R), as listed at the bottom of Figure 1 (more details in Table S1, Supporting Information).

The other details, regarding the chemicals used, the physical and electrochemical characterizations of the synthesized samples, and the hydrogen evolution reaction (HER) activity measurements, are described in the Supporting Information.

■ ASSOCIATED CONTENT

Supporting Information

The Supporting Information is available free of charge at https://pubs.acs.org/doi/10.1021/acsanm.0c03274.

Experimental details (chemicals, characterizations); equations used to calculate the measured parameters; tables for the numerical analysis of XPS spectroscopic and HER electrocatalytic data; Raman spectra; comparison table for HER performance with the reported literature; and figures for the supporting studies (PDF)

https://dx.doi.org/10.1021/acsanm.0c03274
ACS Appl. Nano Mater. XXXX, XXX, XXX−XXX

AUTHOR INFORMATION

Corresponding Author

Pagona Papakonstantinou − *School of Engineering, Engineering Research Institute, Ulster University, Newtownabbey BT37 0QB, United Kingdom;* orcid.org/0000-0003-0019-3247; Email: p.papakonstantinou@ulster.ac.uk

Authors

Shanmughasundaram Duraisamy − *School of Engineering, Engineering Research Institute, Ulster University, Newtownabbey BT37 0QB, United Kingdom*

Abhijit Ganguly − *School of Engineering, Engineering Research Institute, Ulster University, Newtownabbey BT37 0QB, United Kingdom;* orcid.org/0000-0002-8852-2721

Preetam Kumar Sharma − *School of Engineering, Engineering Research Institute, Ulster University, Newtownabbey BT37 0QB, United Kingdom;* orcid.org/0000-0002-5694-8445

John Benson − *2-DTech, Core Technology Facility, Manchester M13 9NT, United Kingdom*

James Davis − *School of Engineering, Engineering Research Institute, Ulster University, Newtownabbey BT37 0QB, United Kingdom;* orcid.org/0000-0003-4284-4431

Complete contact information is available at: https://pubs.acs.org/10.1021/acsanm.0c03274

Author Contributions

[§]S.D. and A.G. contributed equally to this work.

Notes

The authors declare no competing financial interest.

ACKNOWLEDGMENTS

The work was funded by the Department for the Economy in Northern Ireland and Ulster University (provision of Ph.D. studentship to S.D.) and by INVEST Northern Ireland, Biodevices grant with Ref RD0714186.

REFERENCES

(1) Zou, X.; Zhang, Y. Noble Metal-Free Hydrogen Evolution Catalysts for Water Splitting. *Chem. Soc. Rev.* **2015**, *44*, 5148−5180.

(2) Eda, G.; Yamaguchi, H.; Voiry, D.; Fujita, T.; Chen, M.; Chhowalla, M. Photoluminescence from Chemically Exfoliated MoS2. *Nano Lett.* **2011**, *11*, 5111−5116.

(3) Lin, Y.-C.; Dumcenco, D. O.; Huang, Y.-S.; Suenaga, K. Atomic Mechanism of the Semiconducting-to-Metallic Phase Transition in Single-Layered MoS2. *Nat. Nanotechnol.* **2014**, *9*, 391−396.

(4) Duerloo, K.-A. N.; Li, Y.; Reed, E. J. Structural Phase Transitions in Two-Dimensional Mo- and W-Dichalcogenide Monolayers. *Nat. Commun.* **2014**, No. 4214.

(5) Voiry, D.; Mohite, A.; Chhowalla, M. Phase Engineering of Transition Metal Dichalcogenides. *Chem. Soc. Rev.* **2015**, *44*, 2702−2712.

(6) Li, H.; Tsai, C.; Koh, A. L.; Cai, L.; Contryman, A. W.; Fragapane, A. H.; Zhao, J.; Han, H. S.; Manoharan, H. C.; Abild-Pedersen, F.; Nørskov, J. K.; Zheng, X. Activating and Optimizing MoS2 Basal Planes for Hydrogen Evolution through the Formation of Strained Sulphur Vacancies. *Nat. Mater.* **2016**, *15*, 48−53.

(7) Wang, J.; Wang, N.; Guo, Y.; Yang, J.; Wang, J.; Wang, F.; Sun, J.; Xu, H.; Liu, Z.-H.; Jiang, R. Metallic-Phase MoS2 Nanopetals with Enhanced Electrocatalytic Activity for Hydrogen Evolution. *ACS Sustainable Chem. Eng.* **2018**, *6*, 13435−13442.

(8) Wang, C.; Wang, H.; Lin, Z.; Li, W.; Lin, B.; Qiu, W.; Quan, Y.; Liu, Z.; Chen, S. In Situ Synthesis of Edge-Enriched MoS2 Hierarchical Nanorods with 1T/2H Hybrid Phases for Highly Efficient Electrocatalytic Hydrogen Evolution. *CrystEngComm* **2019**, *21*, 1984−1991.

(9) Jaramillo, T. F.; Jørgensen, K. P.; Bonde, J.; Nielsen, J. H.; Horch, S.; Chorkendorff, I. Identification of Active Edge Sites for Electrochemical H2 Evolution from MoS2 Nanocatalysts. *Science* **2007**, *317*, 100−102.

(10) Yin, Y.; Han, J.; Zhang, Y.; Zhang, X.; Xu, P.; Yuan, Q.; Samad, L.; Wang, X.; Wang, Y.; Zhang, Z.; Zhang, P.; Cao, X.; Song, B.; Jin, S. Contributions of Phase, Sulfur Vacancies, and Edges to the Hydrogen Evolution Reaction Catalytic Activity of Porous Molybdenum Disulfide Nanosheets. *J. Am. Chem. Soc.* **2016**, *138*, 7965−7972.

(11) Cai, L.; He, J.; Liu, Q.; Yao, T.; Chen, L.; Yan, W.; Hu, F.; Jiang, Y.; Zhao, Y.; Hu, T.; Sun, Z.; Wei, S. Vacancy-Induced Ferromagnetism of MoS2 Nanosheets. *J. Am. Chem. Soc.* **2015**, *137*, 2622−2627.

(12) Shi, S.; Gao, D.; Xia, B.; Liu, P.; Xue, D. Enhanced Hydrogen Evolution Catalysis in MoS2 Nanosheets by Incorporation of a Metal Phase. *J. Mater. Chem. A* **2015**, *3*, 24414−24421.

(13) Zhang, C.; Jiang, L.; Zhang, Y.; Hu, J.; Leung, M. K. H. Janus Effect of O2 Plasma Modification on the Electrocatalytic Hydrogen Evolution Reaction of MoS2. *J. Catal.* **2018**, *361*, 384−392.

(14) Zheng, Z.; Yu, L.; Gao, M.; Chen, X.; Zhou, W.; Ma, C.; Wu, L.; Zhu, J.; Meng, X.; Hu, J.; Tu, Y.; Wu, S.; Mao, J.; Tian, Z.; Deng, D. Boosting Hydrogen Evolution on MoS2 via Co-Confining Selenium in Surface and Cobalt in Inner Layer. *Nat. Commun.* **2020**, *11*, No. 3315.

(15) Papageorgopoulos, C. A.; Jaegermann, W. Li Intercalation across and along the van Der Waals Surfaces of MoS2(0001). *Surf. Sci.* **1995**, *338*, 83−93.

(16) Chua, C. K.; Loo, A. H.; Pumera, M. Top-Down and Bottom-Up Approaches in Engineering 1 T Phase Molybdenum Disulfide (MoS2): Towards Highly Catalytically Active Materials. *Chem. − Eur. J.* **2016**, *22*, 14336−14341.

(17) Jiao, Y.; Hafez, A. M.; Cao, D.; Mukhopadhyay, A.; Ma, Y.; Zhu, H. Metallic MoS2 for High Performance Energy Storage and Energy Conversion. *Small* **2018**, *14*, No. 1800640.

(18) Maitra, U.; Gupta, U.; De, M.; Datta, R.; Govindaraj, A.; Rao, C. N. R. Highly Effective Visible-Light-Induced H2 Generation by Single-Layer 1T-MoS2 and a Nanocomposite of Few-Layer 2H-MoS2 with Heavily Nitrogenated Graphene. *Angew. Chem., Int. Ed.* **2013**, *52*, 13057−13061.

(19) Liu, Z.; Gao, Z.; Liu, Y.; Xia, M.; Wang, R.; Li, N. Heterogeneous Nanostructure Based on 1T-Phase MoS2 for Enhanced Electrocatalytic Hydrogen Evolution. *ACS Appl. Mater. Interfaces* **2017**, *9*, 25291−25297.

(20) Li, Y.; Wang, L.; Zhang, S.; Dong, X.; Song, Y.; Cai, T.; Liu, Y. Cracked Monolayer 1T MoS2 with Abundant Active Sites for Enhanced Electrocatalytic Hydrogen Evolution. *Catal. Sci. Technol.* **2017**, *7*, 718−724.

(21) Wang, D.; Zhang, X.; Bao, S.; Zhang, Z.; Fei, H.; Wu, Z. Phase Engineering of a Multiphasic 1T/2H MoS2 Catalyst for Highly Efficient Hydrogen Evolution. *J. Mater. Chem. A* **2017**, *5*, 2681−2688.

(22) Venkateshwaran, S.; Senthil Kumar, S. M. Template-Driven Phase Selective Formation of Metallic 1T-MoS2 Nanoflowers for Hydrogen Evolution Reaction. *ACS Sustainable Chem. Eng.* **2019**, *7*, 2008−2017.

(23) Liu, S.; Zhou, L.; Zhang, W.; Jin, J.; Mu, X.; Zhang, S.; Chen, C.; Mu, S. Stabilizing Sulfur Vacancy Defects by Performing "Click" Chemistry of Ultrafine Palladium to Trigger a High-Efficiency Hydrogen Evolution of MoS2. *Nanoscale* **2020**, *12*, 9943−9949.

(24) Xue, X.; Zhang, J.; Saana, I. A.; Sun, J.; Xu, Q.; Mu, S. Rational Inert-Basal-Plane Activating Design of Ultrathin 1T′ Phase MoS2 with a MoO3 Heterostructure for Enhancing Hydrogen Evolution Performances. *Nanoscale* **2018**, *10*, 16531−16538.

(25) Amiinu, I. S.; Pu, Z.; Liu, X.; Owusu, K. A.; Monestel, H. G. R.; Boakye, F. O.; Zhang, H.; Mu, S. Multifunctional Mo−N/C@MoS2 Electrocatalysts for HER, OER, ORR, and Zn−Air Batteries. *Adv. Funct. Mater.* **2017**, *27*, No. 1702300.

(26) Geng, X.; Sun, W.; Wu, W.; Chen, B.; Al-Hilo, A.; Benamara, M.; Zhu, H.; Watanabe, F.; Cui, J.; Chen, T. Pure and Stable Metallic Phase Molybdenum Disulfide Nanosheets for Hydrogen Evolution Reaction. *Nat. Commun.* **2016**, *7*, No. 10672.
(27) Huang, H.; Liu, N.; Wang, X.; Luo, Q.; Huang, X.; Wang, X.; Zhong, M.; Zhang, H. DFT Calculation of Hydrothermal Mechanism on Preparation of MoS2. *J. Mol. Model.* **2020**, *26*, No. 257.
(28) Feldman, Y.; Lyakhovitskaya, V.; Tenne, R. Kinetics of Nested Inorganic Fullerene-like Nanoparticle Formation. *J. Am. Chem. Soc.* **1998**, *120*, 4176−4183.
(29) Luan, B.; Zhou, R. Wettability and Friction of Water on a MoS2 Nanosheet. *Appl. Phys. Lett.* **2016**, *108*, No. 131601.
(30) Acerce, M.; Voiry, D.; Chhowalla, M. Metallic 1T Phase MoS2 Nanosheets as Supercapacitor Electrode Materials. *Nat. Nanotechnol.* **2015**, *10*, 313−318.
(31) Chatti, M.; Gengenbach, T.; King, R.; Spiccia, L.; Simonov, A. N. Vertically Aligned Interlayer Expanded MoS2 Nanosheets on a Carbon Support for Hydrogen Evolution Electrocatalysis. *Chem. Mater.* **2017**, *29*, 3092−3099.
(32) Geng, X.; Sun, W.; Wu, W.; Chen, B.; Al-Hilo, A.; Benamara, M.; Zhu, H.; Watanabe, F.; Cui, J.; Chen, T. P. Pure and Stable Metallic Phase Molybdenum Disulfide Nanosheets for Hydrogen Evolution Reaction. *Nat. Commun.* **2016**, *7*, No. 10672.
(33) Shang, L.; Williams-Jones, A. E.; Wang, X.; Timofeev, A.; Hu, R.; Bi, X. An Experimental Study of the Solubility and Speciation of MoO3(s) in Hydrothermal Fluids at Temperatures up to 350 °C. *Econ. Geol.* **2020**, *115*, 661−669.
(34) Dadze, T. P.; Kashirtseva, G. A.; Novikov, M. P.; Plyasunov, A. V. Solubility of MoO3 in Acid Solutions and Vapor-Liquid Distribution of Molybdic Acid. *Fluid Phase Equilib.* **2017**, *440*, 64−76.
(35) Sokolikova, M. S.; Mattevi, C. Direct Synthesis of Metastable Phases of 2D Transition Metal Dichalcogenides. *Chem. Soc. Rev.* **2020**, *49*, 3952−3980.
(36) Xie, J.; Zhang, H.; Li, S.; Wang, R.; Sun, X.; Zhou, M.; Zhou, J.; Lou, X. W.; Xie, Y. Defect-Rich MoS2 Ultrathin Nanosheets with Additional Active Edge Sites for Enhanced Electrocatalytic Hydrogen Evolution. *Adv. Mater.* **2013**, *25*, 5807−5813.
(37) Muralikrishna, S.; Manjunath, K.; Samrat, D.; Reddy, V.; Ramakrishnappa, T.; Nagaraju, D. H. Hydrothermal Synthesis of 2D MoS2 Nanosheets for Electrocatalytic Hydrogen Evolution Reaction. *RSC Adv.* **2015**, *5*, 89389−89396.
(38) Cai, L.; Cheng, W.; Yao, T.; Huang, Y.; Tang, F.; Liu, Q.; Liu, W.; Sun, Z.; Hu, F.; Jiang, Y.; Yan, W.; Wei, S. High-Content Metallic 1T Phase in MoS2-Based Electrocatalyst for Efficient Hydrogen Evolution. *J. Phys. Chem. C* **2017**, *121*, 15071−15077.
(39) Joensen, P.; Crozier, E. D.; Alberding, N.; Frindt, R. F. A study of single-layer and restacked MoS_2 by X-ray diffraction and X-ray absorption spectroscopy. *J. Phys. C: Solid State Phys.* **1987**, *20*, 4043−4053.
(40) Yang, L.; Cui, X.; Zhang, J.; Wang, K.; Shen, M.; Zeng, S.; Dayeh, S. A.; Feng, L.; Xiang, B. Lattice Strain Effects on the Optical Properties of MoS2 Nanosheets. *Sci. Rep.* **2015**, *4*, No. 5649.
(41) Leng, X.; Wang, Y.; Wang, F. Alcohols Assisted Hydrothermal Synthesis of Defect-Rich MoS2 and Their Applications in Humidity Sensing. *Adv. Mater. Interfaces* **2019**, *6*, No. 1900010.
(42) Liu, Q.; Li, X.; He, Q.; Khalil, A.; Liu, D.; Xiang, T.; Wu, X.; Song, L. Gram-Scale Aqueous Synthesis of Stable Few-Layered 1T-MoS2: Applications for Visible-Light-Driven Photocatalytic Hydrogen Evolution. *Small* **2015**, *11*, 5556−5564.
(43) Jiménez Sandoval, S.; Yang, D.; Frindt, R. F.; Irwin, J. C. Raman Study and Lattice Dynamics of Single Molecular Layers of MoS2. *Phys. Rev. B* **1991**, *44*, 3955−3962.
(44) Sinaim, H.; Ham, D. J.; Lee, J. S.; Phuruangrat, A.; Thongtem, S.; Thongtem, T. Free-Polymer Controlling Morphology of α-MoO3 Nanobelts by a Facile Hydrothermal Synthesis, Their Electrochemistry for Hydrogen Evolution Reactions and Optical Properties. *J. Alloys Compd.* **2012**, *516*, 172−178.
(45) Kibsgaard, J.; Chen, Z.; Reinecke, B. N.; Jaramillo, T. F. Engineering the Surface Structure of MoS2 to Preferentially Expose Active Edge Sites for Electrocatalysis. *Nat. Mater.* **2012**, *11*, 963−969.
(46) Jia, Y.; Yang, Q.; Sun, S.; Nie, H.; Li, D. The Influence of Metal Deposits on Residue Hydrodemetallization Catalysts in the Absence and Presence of Coke. *Energy Fuels* **2016**, *30*, 2544−2554.
(47) Huang, H.; Cui, Y.; Li, Q.; Dun, C.; Zhou, W.; Huang, W.; Chen, L.; Hewitt, C. A.; Carroll, D. L. Metallic 1T Phase MoS2 Nanosheets for High-Performance Thermoelectric Energy Harvesting. *Nano Energy* **2016**, *26*, 172−179.
(48) Li, H.; Yu, K.; Tang, Z.; Fu, H.; Zhu, Z. High Photocatalytic Performance of a Type-II α-MoO3@MoS2 Heterojunction: From Theory to Experiment. *Phys. Chem. Chem. Phys.* **2016**, *18*, 14074−14085.
(49) Curry, J. F.; Wilson, M. A.; Luftman, H. S.; Strandwitz, N. C.; Argibay, N.; Chandross, M.; Sidebottom, M. A.; Krick, B. A. Impact of Microstructure on MoS2 Oxidation and Friction. *ACS Appl. Mater. Interfaces* **2017**, *9*, 28019−28026.
(50) Afanasiev, P.; Lorentz, C. Oxidation of Nanodispersed MoS2 in Ambient Air: The Products and the Mechanistic Steps. *J. Phys. Chem. C* **2019**, *123*, 7486−7494.
(51) Escalera-López, D.; Lou, Z.; Rees, N. V. Benchmarking the Activity, Stability, and Inherent Electrochemistry of Amorphous Molybdenum Sulfide for Hydrogen Production. *Adv. Energy Mater.* **2019**, *9*, No. 1802614.
(52) Zhang, X.-H.; Li, N.; Wu, J.; Zheng, Y.-Z.; Tao, X. Defect-Rich O-Incorporated 1T-MoS2 Nanosheets for Remarkably Enhanced Visible-Light Photocatalytic H2 Evolution over CdS: The Impact of Enriched Defects. *Appl. Catal., B* **2018**, *229*, 227−236.
(53) Luo, Z.; Miao, R.; Huan, T. D.; Mosa, I. M.; Poyraz, A. S.; Zhong, W.; Cloud, J. E.; Kriz, D. A.; Thanneeru, S.; He, J.; Zhang, Y.; Ramprasad, R.; Suib, S. L. Mesoporous MoO3−x Material as an Efficient Electrocatalyst for Hydrogen Evolution Reactions. *Adv. Energy Mater.* **2016**, *6*, No. 1600528.
(54) Phuruangrat, A.; Ham, D. J.; Thongtem, S.; Lee, J. S. Electrochemical Hydrogen Evolution over MoO3 Nanowires Produced by Microwave-Assisted Hydrothermal Reaction. *Electrochem. commun.* **2009**, *11*, 1740−1743.
(55) Liu, W.; Benson, J.; Dawson, C.; Strudwick, A.; Raju, A. P. A.; Han, Y.; Li, M.; Papakonstantinou, P. The Effects of Exfoliation, Organic Solvents and Anodic Activation on the Catalytic Hydrogen Evolution Reaction of Tungsten Disulfide. *Nanoscale* **2017**, *9*, 13515−13526.
(56) Yang, L.; Zhu, X.; Xiong, S.; Wu, X.; Shan, Y.; Chu, P. K. Synergistic WO3·2H2O Nanoplates/WS2 Hybrid Catalysts for High-Efficiency Hydrogen Evolution. *ACS Appl. Mater. Interfaces* **2016**, *8*, 13966−13972.
(57) Xie, J.; Zhang, J.; Li, S.; Grote, F.; Zhang, X.; Zhang, H.; Wang, R.; Lei, Y.; Pan, B.; Xie, Y. Controllable Disorder Engineering in Oxygen-Incorporated MoS2 Ultrathin Nanosheets for Efficient Hydrogen Evolution. *J. Am. Chem. Soc.* **2013**, *135*, 17881−17888.
(58) Zhou, J.; Fang, G.; Pan, A.; Liang, S. Oxygen-Incorporated MoS2 Nanosheets with Expanded Interlayers for Hydrogen Evolution Reaction and Pseudocapacitor Applications. *ACS Appl. Mater. Interfaces* **2016**, *8*, 33681−33689.
(59) Chen, Z.; Cummins, D.; Reinecke, B. N.; Clark, E.; Sunkara, M. K.; Jaramillo, T. F. Core−Shell MoO3−MoS2 Nanowires for Hydrogen Evolution: A Functional Design for Electrocatalytic Materials. *Nano Lett.* **2011**, *11*, 4168−4175.
(60) Benson, J.; Li, M.; Wang, S.; Wang, P.; Papakonstantinou, P. Electrocatalytic Hydrogen Evolution Reaction on Edges of a Few Layer Molybdenum Disulfide Nanodots. *ACS Appl. Mater. Interfaces* **2015**, *7*, 14113−14122.
(61) McCrory, C. C. L.; Jung, S.; Peters, J. C.; Jaramillo, T. F. Benchmarking Heterogeneous Electrocatalysts for the Oxygen Evolution Reaction. *J. Am. Chem. Soc.* **2013**, *135*, 16977−16987.
(62) Lim, K. R. G.; Handoko, A. D.; Johnson, L. R.; Meng, X.; Lin, M.; Subramanian, G. S.; Anasori, B.; Gogotsi, Y.; Vojvodic, A.; Seh, Z. W. 2H-MoS2 on Mo2CTx MXene Nanohybrid for Efficient and

https://dx.doi.org/10.1021/acsanm.0c03274
ACS Appl. Nano Mater. XXXX, XXX, XXX−XXX

Durable Electrocatalytic Hydrogen Evolution. *ACS Nano* **2020**, *14*, 16140−16155.
(63) Hu, J.; Zhang, C.; Zhang, Y.; Yang, B.; Qi, Q.; Sun, M.; Zi, F.; Leung, M. K. H.; Huang, B. Interface Modulation of MoS2/Metal Oxide Heterostructures for Efficient Hydrogen Evolution Electrocatalysis. *Small* **2020**, *16*, No. 2002212.
(64) Hu, J.; Zhang, C.; Yang, P.; Xiao, J.; Deng, T.; Liu, Z.; Huang, B.; Leung, M. K. H.; Yang, S. Kinetic-Oriented Construction of MoS2 Synergistic Interface to Boost PH-Universal Hydrogen Evolution. *Adv. Funct. Mater.* **2020**, *30*, No. 1908520.
(65) Liu, J.; Wang, Z.; Li, J.; Cao, L.; Lu, Z.; Zhu, D. Structure Engineering of MoS2 via Simultaneous Oxygen and Phosphorus Incorporation for Improved Hydrogen Evolution. *Small* **2020**, *16*, No. 1905738.
(66) Lu, Z.; Zhu, W.; Yu, X.; Zhang, H.; Li, Y.; Sun, X.; Wang, X.; Wang, H.; Wang, J.; Luo, J.; Lei, X.; Jiang, L. Ultrahigh Hydrogen Evolution Performance of Under-Water "Superaerophobic" MoS2 Nanostructured Electrodes. *Adv. Mater.* **2014**, *26*, 2683−2687.
(67) Jeon, D.; Park, J.; Shin, C.; Kim, H.; Jang, J. W.; Lee, D. W.; Ryu, J. Superaerophobic Hydrogels for Enhanced Electrochemical and Photoelectrochemical Hydrogen Production. *Sci. Adv.* **2020**, *6*, No. eaaz3944.

https://dx.doi.org/10.1021/acsanm.0c03274
ACS Appl. Nano Mater. XXXX, XXX, XXX−XXX